Supplementary Information

Room-temperature nonlinear transport and microwave rectification in antiferromagnetic $MnBi_2Te_4$ films

Shanshan Liu[1#], Rhonald Burgos[2#], Enze Zhang[3], Naizhou Wang[4], Xiao-Bin Qiang[5], Chuanzhao Li,[6] Qihan Zhang[7], , Z. Z. Du[5], Rui Zheng[1], Jingsheng Che[7], Qing-Hua Xu[1], Kai Leng,[6] Weibo Gao[4], Faxian Xiu[3], Dimitrie Culcer[2], Kian Ping Loh[1*]*

[1]Department of Chemistry, National University of Singapore, Singapore 117543, Singapore

[2]School of Physics, The University of New South Wales, Sydney 2052, Australia

[3]State Key Laboratory of Surface Physics and Department of Physics, Fudan University, Shanghai 200433, China

[4]Division of Physics and Applied Physics, School of Physical and Mathematical Sciences, Nanyang Technological University, Singapore 637371, Singapore

[5]Shenzhen Institute for Quantum Science and Engineering and Department of Physics, Southern University of Science and Technology (SUSTech), Shenzhen 518055, China.

[6]Department of Applied Physics, The Hong Kong Polytechnic University, Kowloon 999077 Hong Kong, China

[7]Department of Materials Science and Engineering, National University of Singapore, Singapore, 117575, Singapore

Content:

Supplementary Note 1. Theory for the nonlinear transverse response in $MnBi_2Te_4$

1.1 Scaling behavior and nonlinear transverse conductivity

The nonlinear transverse conductivity response $\sigma_{yxx}^{2\omega}$ observed in the experiment presents a particular behavior as a function of the linear longitudinal conductivity σ_{xx}. The linear response conductivity is known to scale as $\sigma_{xx} \sim \tau_{imp}$ where τ_{imp} is a phenomenological relaxation time that scales inversely proportional to impurity density. Experimental results show that the non-linear transverse response behaves as with $\sigma_{yxx}^{2\omega} \sim C_1\tau_{imp} + C_2{\tau_{imp}}^3$, with C_1 and C_2 of Fermi-energy-dependent prefactors. Here we explain that behavior.

We will use an effective Hamiltonian that includes warping as $H = H_0 + H_E + U(r)$. The unperturbed Hamiltonian H_0 is the band Hamiltonian including hexagonal warping and a gap parameter, H_E is the external driving field and $U(r)$ represents the disorder scattering potential. The unperturbed band Hamiltonian is

$$H_0 = \hbar v_F\left(k_x\sigma_y - k_y\sigma_x\right) + i\frac{\lambda}{2}(k_+^3 - k_-^3)\sigma_z + \Delta\sigma_z\,, \qquad (1)$$

with the definition $k_\pm = k_x \pm ik_y$. Also, λ is the warping parameter and Δ is the gap of the system. For the disorder model, we will consider two independent sources. One that dominates the relaxation process is the ordinary scalar scattering $U_0(r)$ whose correlation gives rise to a relaxation time τ and one that is related to the extrinsic spin-orbit impurity scattering which can be cast as $U = i\beta\vec{k}\times\vec{k}'$. This last one will give a relaxation process that we will call γ_β. Including only one source of scattering will provide at most a non-linear response that scales as $\sigma_{yxx}^{2\omega} \sim {\tau_{imp}}^2$.[1] This can in principle be interpreted as a quantity that scales as $\sigma_{yxx}^{2\omega} \sim {\sigma_{xx}}^2$. Hence it cannot be a satisfactory explanation for the observed experimental trends. Including the other source of disorder, will give a second-order leading response that scales as $\sigma_{yxx}^{2\omega} \sim {\tau_{imp}}^3$and this can be interpreted as something that scales with the linear conductivity as $\sigma_{yxx}^{2\omega} \sim {\sigma_{xx}}^3$.

Our approach is based on the solution of the quantum Liouville equation[2,3]. The first step is the solution of the well-known linear response Boltzmann equation that will provide a band diagonal distribution $n_{Ek}^{(-1)mm}$. The super index (-1) means that the distribution scales inversely proportional to impurity density or equivalently proportional to some relaxation time. Once this linear distribution is known, we can calculate the non-linear distribution

$$[J_0(n_{E2}^{(-2)})]^{mm} = \frac{eE_i}{\hbar}\frac{\partial n_{Ek}^{(-1)mm}}{\partial k_i} \ . \qquad (2)$$

Once we calculate the distribution $n_{E2}^{(-2)}$ we can use it to generate a new driving term. This follows from the collision integral of extrinsic spin-orbit coupling impurities. Then the next step is to solve the kinetic equation $[J_0(n_{E2\beta}^{(-2)})]^{mm} = -[J_\beta(n_{E2}^{(-2)})]^{mm}$. The non-linear distribution $n_{E2}^{(-2)}$ provides the current density $j_{\mathrm{y}} = \sigma_{\mathrm{yxx}}^{2\omega} E_{\mathrm{x}}^2$, which gives rise to a response that scales as $\sigma_{\mathrm{yxx}}^{2\omega} \sim {\sigma_{\mathrm{xx}}}^3$.

The response that scales linearly in relaxation time is not trivial since it encompasses side jump and skew scattering effects, both of them generated by an electric field correction of the collision integral[1,2]. Basically we need to calculate a linear side-jump-like distribution from the kinetic equation $[J_0(n_{E\beta}^{(0)})]^{mm} = -[J_{E\beta}(n_{FD}^{(0)})]^{mm}$ and once $n_{E\beta}^{(0)}$ is determined, we can use it to generate non-linear side jump and skew scattering like effect following the steps described previously[1], where explicit expression for the collision integrals $[J_{E\beta}(n_{FD}^{(0)})]$ are also shown. After a lengthy algebra, we find that the non-linear transverse response can be cast as

$$\sigma_{\mathrm{yxx}}^{2\omega} = \lambda \frac{e^3}{\hbar}\frac{\rho(\varepsilon_{\mathrm{F}})}{\varepsilon_{\mathrm{F}}}(1-\xi_{\mathrm{F}}^2)\gamma_\beta[\tau_{\mathrm{imp}} H(\xi_{\mathrm{F}}) + {\tau_{\mathrm{imp}}}^3 \left(\frac{\varepsilon_{\mathrm{F}}}{\hbar}\right)^2 G(\xi_{\mathrm{F}})] \ , \qquad (3)$$

where $H(\xi_F)$ and $G(\xi_F)$ are dimensionless functions of the parameter $\xi_{\mathrm{F}} = \frac{\Delta}{\varepsilon_{\mathrm{F}}}$, The constant relaxation time is defined as $\frac{1}{\tau_{\mathrm{imp}}} = u_0^2 \pi \rho(\varepsilon_{\mathrm{F}})/\hbar$, where u_0^2 takes into account the disorder strength. The parameter $\gamma_\beta = \beta^2 u_0^2 \pi k_{\mathrm{F}}^4 \rho(\varepsilon_{\mathrm{F}})/\hbar$ and the density of states $\rho(\varepsilon_{\mathrm{F}}) = \varepsilon_{\mathrm{F}}/2\pi\hbar^2 v_{\mathrm{F}}^2$. The functions of $H(\xi_{\mathrm{F}})$ and $G(\xi_{\mathrm{F}})$ can be written as:

$$H(\xi_{\mathrm{F}}) = \frac{4}{512}[(1-\xi_{\mathrm{F}}^2)(-10\xi_{\mathrm{F}}^3 - 54\xi_{\mathrm{F}}^5 + 36\xi_{\mathrm{F}}^7) - (1-\xi_{\mathrm{F}}^2)^{1/2}(-88\xi_{\mathrm{F}}^3 + 128\xi_{\mathrm{F}}^5 - 24\xi_{\mathrm{F}}^7)] \ , \qquad (4)$$

$$G(\xi_{\mathrm{F}}) = \frac{1}{64}[15\xi_{\mathrm{F}} + 13\xi_{\mathrm{F}}^3 - 75\xi_{\mathrm{F}}^5 + 33\xi_{\mathrm{F}}^7] \ , \qquad (5)$$

For a general alignment of the axes non-linear transverse response can be written as

$$\sigma_{\mathrm{yxx}}^{2\omega} = \lambda \frac{e^3}{\hbar}\frac{\rho(\varepsilon_{\mathrm{F}})}{\varepsilon_{\mathrm{F}}}(1-\xi_{\mathrm{F}}^2)\gamma_\beta[\tau_{\mathrm{imp}} \mathrm{H}(\xi_{\mathrm{F}}) + {\tau_{\mathrm{imp}}}^3 \left(\frac{\varepsilon_{\mathrm{F}}}{\hbar}\right)^2 G(\xi_{\mathrm{F}})] \cos 3\varphi \ , \qquad (6)$$

$$= \gamma_\beta\left(C_1 \tau_{\mathrm{imp}} + C_2 {\tau_{\mathrm{imp}}}^3\right) \cos 3\varphi \ , \qquad (7)$$

where φ is the angle between the current and x-axis, τ_{imp} is the momentum relaxation time, and C_1 and C_2 are the coefficients.

1.2 Temperature effects

The temperature dependence of the nonlinear susceptibility can be approximated by changing to a modified relaxation time ${\tau_{\rm p}}^{-1} \to {\tau_{\rm imp}}^{-1} + {\tau_{\rm ep}}^{-1}$, namely by using Matthiessen's rule. At high temperatures the electron-phonon scattering time follows the equation[4]

$$\frac{1}{\tau_{\rm ep}} = \frac{2\pi}{\hbar}\sum_q |D_q| \left(\frac{k_{\rm B}T}{\hbar\omega_q}\right) \delta(\hbar\omega_q + \varepsilon_{k-q} - \varepsilon_k)(1 - \cos\theta_{k,k-q}) + \frac{2\pi}{\hbar}\sum_q \sum_q |D_q| \left(\frac{k_B T}{\hbar\omega_q}\right) \delta(\hbar\omega_q + \varepsilon_k - \varepsilon_{k+q})(1 - \cos\theta_{k,k+q}) , \quad (8)$$

where $\hbar\omega_q$ is the energy of the phonon. We take[5]

$$D_q = \alpha \sqrt{\frac{C}{qA}} \left(\frac{\omega_q}{c_{\rm l}}\right)^2 \sqrt{\frac{\hbar}{2\rho_M \omega_q}} , \quad (9)$$

$$\frac{1}{\tau_{\rm ep}} = C\,\frac{1}{\pi}\left(\frac{k_{\rm B}T}{\hbar}\right)\left(\frac{c_{\rm R}}{c_{\rm l}}\right)^4 \left(\frac{1}{2\eta\rho_M c_{\rm R}^2}\right)\left(\frac{\alpha^2}{\hbar^2}\right)(2k_{\rm F}) , \quad (10)$$

where α accounts for the strength of electron-phonon interaction, A is the area of the unit cell, C is determined from the longitudinal $c_{\rm l}$ and transverse $c_{\rm t}$ phonon velocities, $\omega_q = c_{\rm R} q$ is the phonon frequency, $c_{\rm R}$ is velocity and $\rho_{\rm M}$ is the mass density of the material[5].

In our calculation, we approximated the dispersion relation in the delta function to a parabolic one $\varepsilon = \eta\hbar^2 k^2$. Then, the parameter $\frac{1}{\eta} = \Delta / v_{\rm F}^2$ is an effective mass. For an estimation of the value of $1/\tau_{\rm ep}$ for a gap of $2\Delta = 30$ meV, a Fermi energy of $\varepsilon_{\rm F} =$ 30 meV, we get $\frac{1}{\tau_{\rm ep}} = 1.44 \times 10^{10}$ T/sK. For typical values of impurity relaxation times $\tau_{\rm imp} = 1$ ps, we get $\frac{\tau_{\rm imp}}{\tau_{\rm ep}} \sim 10^{-2}$ T/K. Temperature is measured in Kelvin (K).

We recall that in the equation for the nonlinear conductivity $\sigma_{\rm yxx}^{2\omega}$, the factor γ_β is also a relaxation process related to the impurity potential U_β. So we include the effect of phonons in this mechanism by means of Matthiessen's rule. Then, for the fitting process, we can use the equation

$$\sigma_{\rm yxx}^{2\omega} = (1 + BT)\left[\frac{C_1}{(1+AT)} + \frac{C_2}{(1+AT)^3}\right] , \quad (11)$$

where C_1 and C_2 are constant. The factor (1+AT) follows by using $\frac{1}{\tau_{\rm p}} \to \frac{1}{\tau_{\rm imp}} + \frac{1}{\tau_{\rm ep}}$ and factorizing $\frac{1}{\tau_{\rm imp}}$. Similarly, we find the factor (1+BT) by using $\gamma_\beta \to \gamma_\beta + \frac{1}{\tau_{\rm ep}}$.

Supplementary Note 2. Additional characterization data of $MnBi_2Te_4$ films

Besides the layered structure characterized by transmission electron microscopy (TEM), we also used X-ray diffraction (XRD) to investigate the crystalline quality. Displayed in Supplementary Figure 1a, the series of <003> diffraction peaks confirm

the growth orientation along the c-axis. The zero-field-cooled (ZFC) and field-cooled (FC) magnetization curves of 20 septuple layer (SL) $MnBi_2Te_4$ measured at a field of 1 T were plotted in Supplementary Figure 1b, and consistent with the ZFC-FC measured at 0.5 T, the Néel temperature (T_N) is extracted to be ~23 K. The original magnetization hysteresis loops acquired under out-of-plane (H//c) and in-plane (H//ab) magnetic fields were displayed in Supplementary Figure 1c, with the negative liner background from the diamagnetic Al_2O_3 substrate. Based on these magnetization characterizations, the easy-axis can be determined to be along the c-axis. The asymmetry top and bottom surface interfaces has also been captured in the cross-section TEM results (Supplementary Figure 1d).

The surface broken inversion symmetry of 7 SL, 14 SL and 20 SL $MnBi_2Te_4$ film was also confirmed by the second-harmonic generation (SHG) measurement, as depicted in Supplementary Figure 2. The linear relation between SHG intensity and incident power also suggests its intrinsic origin, and the six-fold pattern in the polar plot suggests its origin of broken surface inversion symmetry[6]. This is consistent with the broken surface inversion symmetry in $MnBi_2Te_4$ as a topological insulator above Néel temperature[7–9].

The A-type antiferromagnetism (AFM) indicated by multiple switching steps was also detected in other thickness samples, and the temperature-dependent anomalous Hall effect data were shown in Supplementary Figure 3. Due to the A-type AFM, the even-layer $MnBi_2Te_4$ should show nearly zero magnetization ideally. However, experimentally many factors can generate an uncompensated magnetization and affect the magnetism characterization, like disorders, or defects in molecular beam epitaxy (MBE)-grown films. The inevitable defects in $MnBi_2Te_4$ have been proved by theoretical calculations and experiments[10–12]. Furthermore, the substrate-induced top-bottom surface asymmetry may also induce a net magnetization[13]. Based on the XRD data and cross-section TEM, displayed in Supplementary Figure 1a and 1d, it can be inferred that the dominant phase in our MBE-grown film is $MnBi_2Te_4$ rather than Mn-doped Bi_2Te_3. Furthermore, Mn-doped Bi_2Te_3 behaves with metallic property[14,15] with the 2D carrier density in the range of 10^{13}-10^{14} cm^{-2} at 4.2 K,[16] roughly two orders higher than that of the semiconducting $MnBi_2Te_4$ films here, which can also help to confirm the dominant $MnBi_2Te_4$ phase in our grown films.

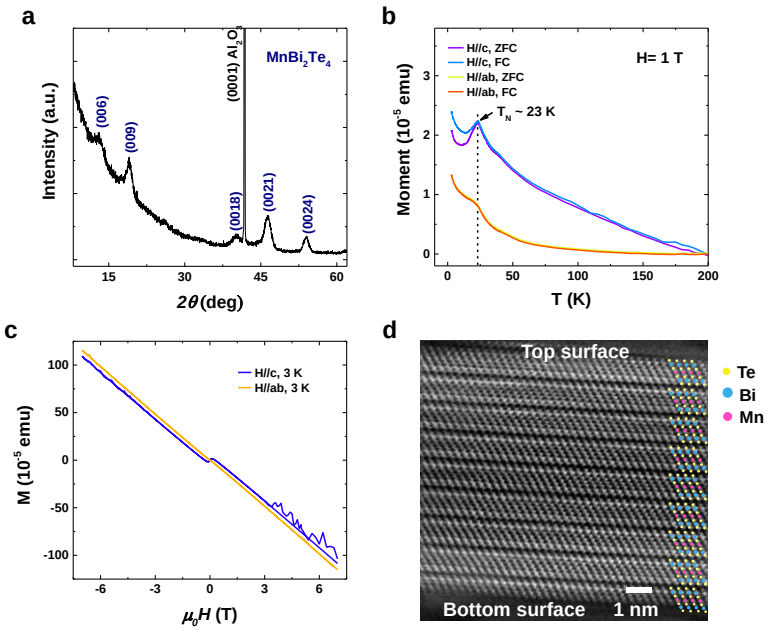

Supplementary Figure 1. Characterization of the epitaxial $MnBi_2Te_4$ film. (a) XRD pattern of 7 SL $MnBi_2Te_4$ film. Additional (b) ZFC-FC magnetization at μ_0H=1 T and (c) original field-dependent magnetization curves of $MnBi_2Te_4$ that displayed in Figure 1c in the main text. (d) Cross-section TEM of $MnBi_2Te_4$ film grown on Al_2O_3 substrate.

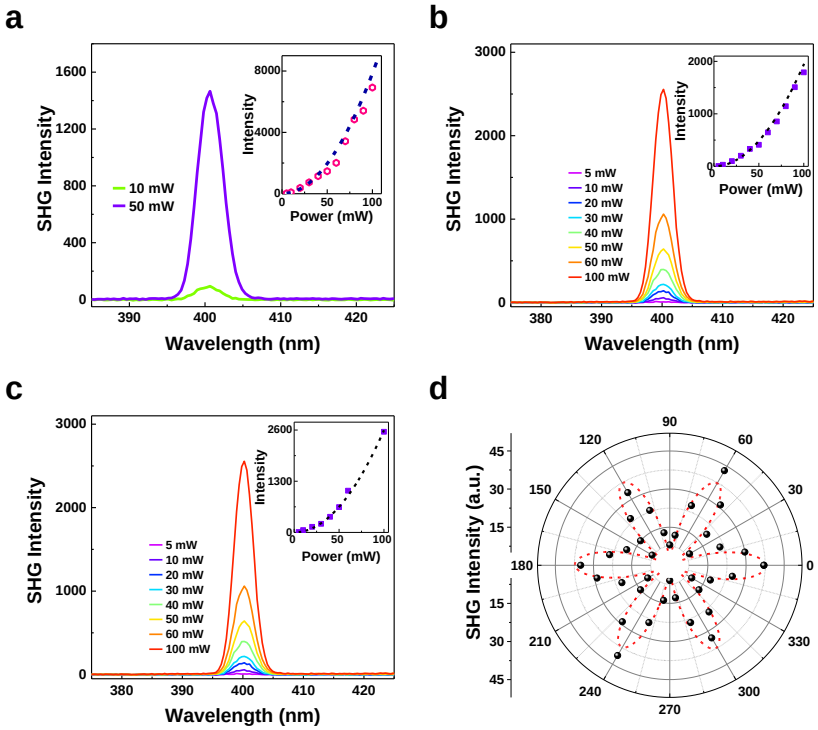

Supplementary Figure 2. Second harmonic generation (SHG) signal of $MnBi_2Te_4$ films at 300 K. SHG of (a) 7 SL, (b) (a) 14 SL, and (c) 20 SL film. Insets, the linear relation between SHG signal and incident power. (d) Polarization-resolved SHG of 20 SL film. The red dash liens are fitting to the equation demonstrated in J.F. et.al[6].

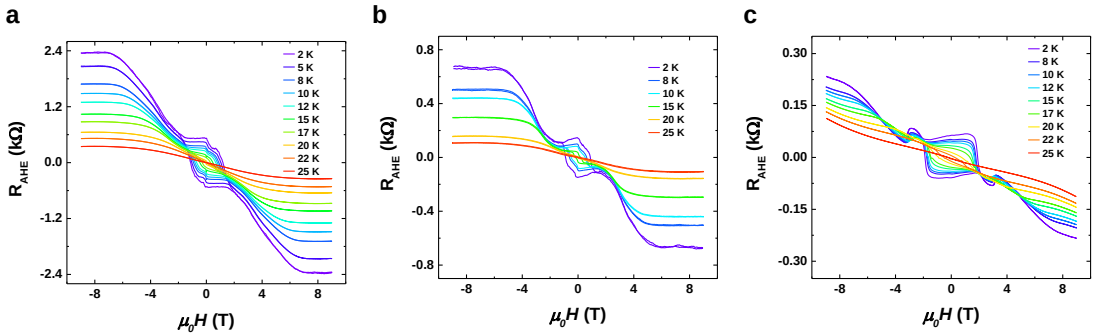

Supplementary Figure 3. Anomalous Hall effects of (a) 8 SL, (b) 14 SL, and (c) 20 SL $MnBi_2Te_4$ film at various temperatures. The A-type antiferromagnetism property is further verified by the multi-step switching process, i.e., spin-flop states.

Supplementary Note 3. Exclusion of other extrinsic origins for nonlinear response

There is an existing ambiguity in the definition of the nonlinear Hall effect. In some references[17–20], it is defined as the antisymmetric component of the nonlinear conductivity tensor. While in other reports[21–23], it is defined as the transverse voltage response. To avoid the ambiguity on the nonlinear Hall effect, we called our nonlinear behavior as nonlinear transport or the nonlinear transverse response through the whole manuscript.

The extrinsic factors that can induce the nonlinear transport transport can be excluded by the control measurements. And here taking 7 SL as an example, we discuss how to exclude the extrinsic effects.

(1) Accidental diode-like contact junction effect. The Schottky contacts between the device and metal electrodes can also induce a rectification effect. The two-terminal *I-V* curves can be used to verify the contact effect. As presented in Supplementary Figure 4, good Ohmic contact across all electrodes was observed as indicated by the linear *I-V* behavior.

(2) Capacitance coupling effect. To exclude the spurious capacitive coupling effects, the frequency-dependent measurements were carried out. Supplementary Figure 5 shows the nonlinear transverse response $V_{xy}^{2\omega}$ as a function of current under various current frequencies. $V_{xy}^{2\omega}$ shows a quadratic dependence on the applied current and no frequency dependence of $V_{xy}^{2\omega}$ was observed in the frequency range of 6-277 Hz, which helps to exclude the capacitance coupling effect.

(3) Thermal and thermoelectric effect from Jolue heating. The Joule heating can cause the temperature change and gradient in the device[24]. However, this effect can be excluded by the angular dependence measurement. Displayed in Supplementary Figure 6b, the three-fold rotation symmetry of $V_{xy}^{2\omega}$ which is consistent with the internal symmetry of $MnBi_2Te_4$ can be used to exclude the

Joule heating effect.

(4) Mixing from the second harmonic longitudinal signals $V_{xx}^{2\omega}$. We measured the second-harmonic transverse and longitudinal voltage simultaneously at 10K, as presented in Figure 2b in the main text. Compared to $V_{xy}^{2\omega}$, $V_{xx}^{2\omega}$ shows an even smaller signal, which can be helpful to exclude such a possibility. Among the whole measured temperature range, $V_{xx}^{2\omega}$ is relatively smaller than $V_{xy}^{2\omega}$, as presented in Supplementary Figure 7.

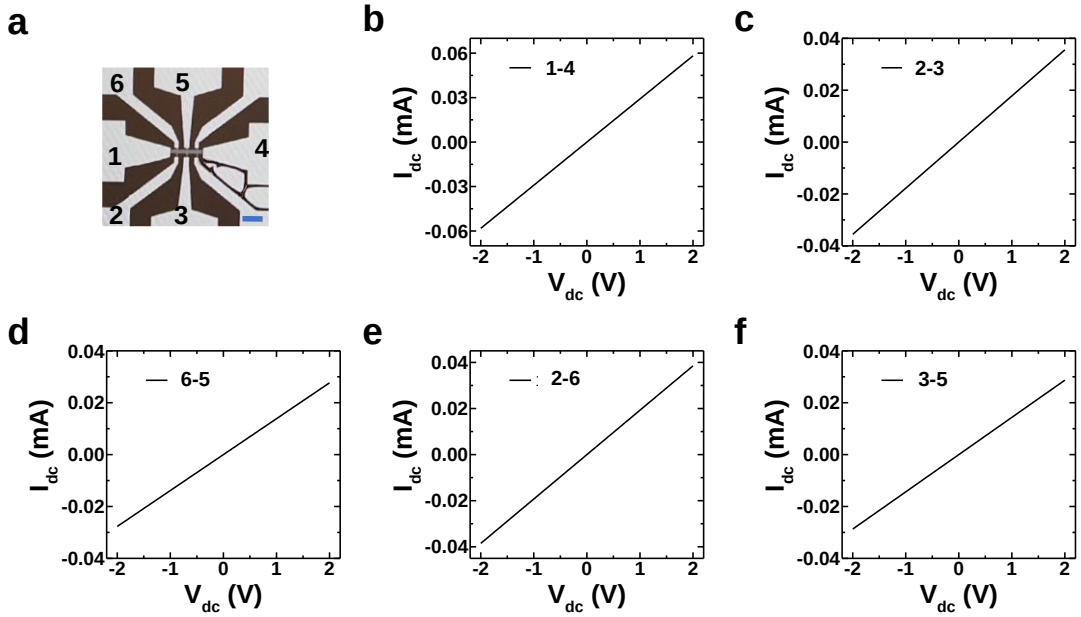

Supplementary Figure 4. Two-terminal measurements in 7 SL $MnBi_2Te_4$ device. (a) Optical image of the Hall-bar device. Scale bar, 50 μm. (b) Two-terminal *I-V* curves for different configurations.

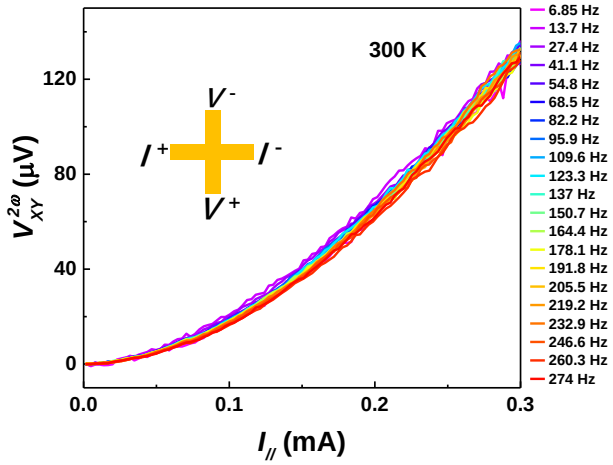

Supplementary Figure 5. Frequency-dependent second-harmonic transverse response $V_{xy}^{2\omega}$ of 7 SL $MnBi_2Te_4$ device.

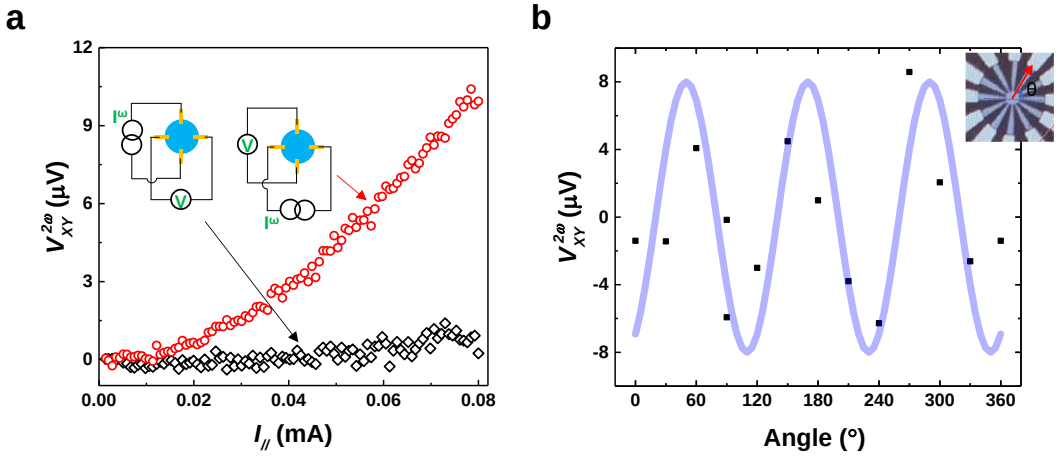

Supplementary Figure 6. Angular dependence of the nonlinear transverse response in 7 SL $MnBi_2Te_4$ device. (a) Second-harmonic transverse response $V_{xy}^{2\omega}$ measured for two opposite measurement geometries at 300 K. (b) $V_{xy}^{2\omega}$ as a function of the current injection angle.

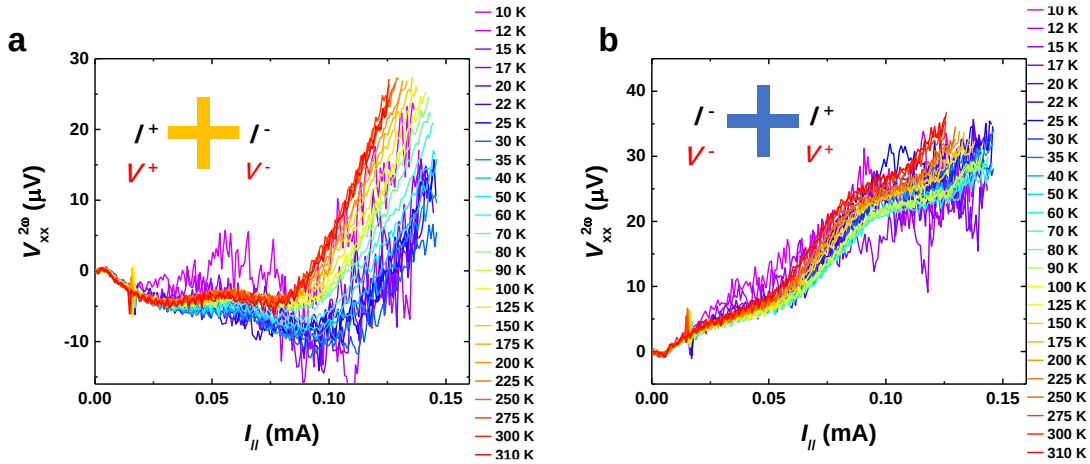

Supplementary Figure 7. Second harmonic response along the longitudinal direction ($V_{xx}^{2\omega}$) in 7 SL $MnBi_2Te_4$ device. (a) and (b) are the temperature-dependent $V_{xx}^{2\omega}$ for two measurement configurations with opposite current directions. No obvious $V_{xx}^{2\omega}$ was detected.

Supplementary Note 4. Room-temperature nonlinear transverse response in different thickness films

To gain a deeper understanding of the origin of the room-temperature nonlinear transverse response in $MnBi_2Te_4$ films, we further explored the nonlinear transverse response in more devices with different thicknesses. Supplementary Figure 8a presents the typical results of 20 SL film measured at two setups with opposite injection currents. The quadratic dependence of $V_{xy}^{2\omega}$ on longitudinal current, combined with a sign

reversal for two opposite measurement setups observed in two distinct measurement setups, indicates its second harmonic origin. To estimate the magnitude of the nonlinear transverse response, we plot the nonlinear transverse signals in the electric field with the equation of $E_{xy}^{2\omega} = \frac{V_{xy}^{2\omega}}{L_{xy}}$ and $E_{//} = \frac{V_{//}}{L_{//}} = \frac{I_{//} \times R_{xx}}{L_{//}}$. Displayed in Supplementary Figure 8b, $E_{xy}^{2\omega}$ depends linearly on $E_{//}^{2}$ in the whole measurement, and the magnitude can be extracted from the slope $\frac{E_{xy}^{2\omega}}{E_{//}^{2}}$. Temperature-dependent nonlinear transverse magnitude and longitudinal conductivity are drawn in Supplementary Figure 8c, which is similar to the result observed in 7 SL device. The overlap of $V_{xy}^{2\omega}$ obtained at various driving AC frequencies (Supplementary Figure 9a) further excludes the extrinsic capacitive coupling effect. The extrinsic factors of contribution from $V_{xx}^{2\omega}$ and Schottky contact can also be excluded by the negligible $V_{xx}^{2\omega}$ (Supplementary Figure 9b-c) and good Ohmic contacts among all electrodes (Supplementary Figure 10). Supplementary Figure 11 is an optical image of 20 SL device with radially distributed electrodes, and $V_{xy}^{2\omega}$ also shows a threefold roration symmetry with the current injection changing which is consistent with the phenomenon in 7 SL device (Supplementary Figure 6b).

The room-temperature nonlinear transverse response can also be detected in 14 SL and 8 SL $MnBi_2Te_4$ films, results are presented in Supplementary Figure 12 and Figure 13, respectively. Supplementary Figure 13d presents the nonlinear transverse signals under three different magnetic states. The initial state with zero magnetization is obtained by directly cooling the sample without a magnetic field applied. Then the magnetic field is scanned from -2.3 T to 0 T to get the AFM-1 state, and the AFM-2 state is prepared by sweeping the magnetic field from 2.3 T to 0 T. Based on the AHE result (Supplementary Figure 3a), the AFM-1 and AFM-2 states possess non-zero but opposite magnetization. However, the nonlinear transverse signals show negligible dependence on the magnetic order, which excludes its origin of the quantum metric dipole effect. The nonlinear response contributed by other mechanisms, like berry curvature dipole, skew scattering, and side jump effects, is irrelevant to the magnetic order.

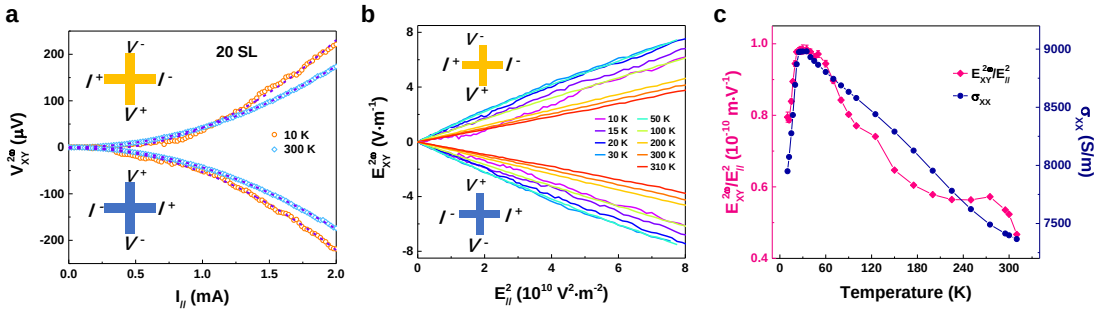

Supplementary Figure 8. Room-temperature nonlinear transverse response in 20 SL $MnBi_2Te_4$ device. (a) Nonlinear transverse response $V_{xy}^{2\omega}$ as a function of current at

10K and 300K for two measurement configurations. Dash lines are the quadratic fittings. (b) Temperature-dependent $E_{xy}^{2\omega}$ versus $E_{//}^{2}$ for two opposite measurement configurations. (c) Nonlinear transverse magnitude $\frac{E_{xy}^{2\omega}}{E_{//}^{2}}$ and longitudinal conductivity as a function of temperature. The error bars are added based on the standard fitting error of $E_{xy}^{2\omega}$ versus $E_{//}^{2}$.

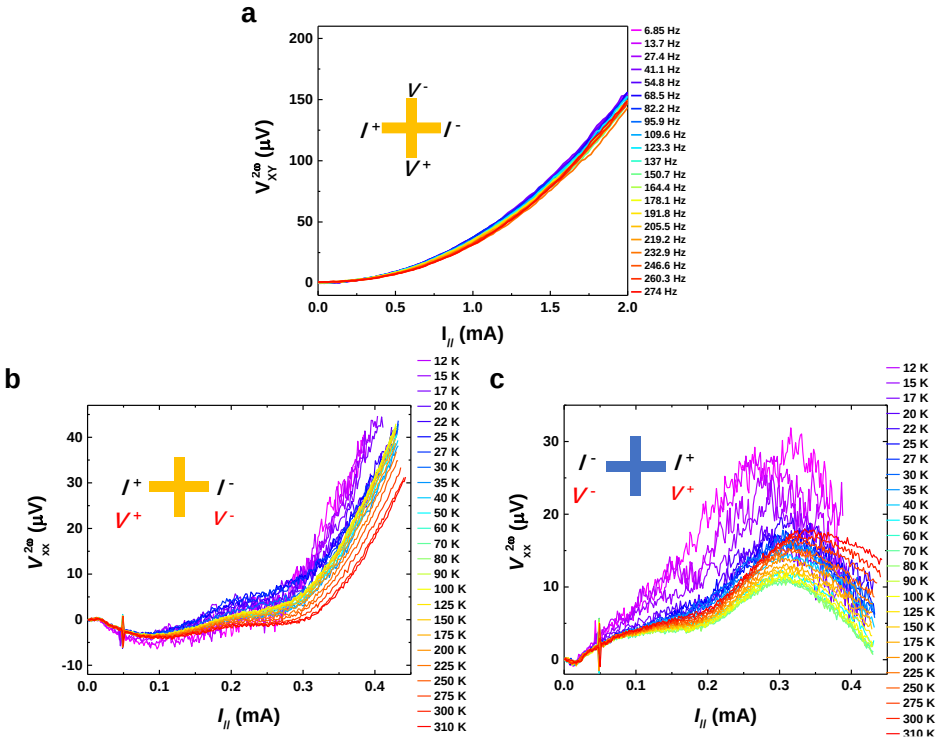

Supplementary Figure 9. Second harmonic response in 20 SL $MnBi_2Te_4$ device. (a) $V_{xy}^{2\omega}$ as a function of applied current at 300 K, acquired for different AC frequencies. (b)-(c) Temperature-dependent $V_{xx}^{2\omega}$ for two measurement configurations with opposite current directions.

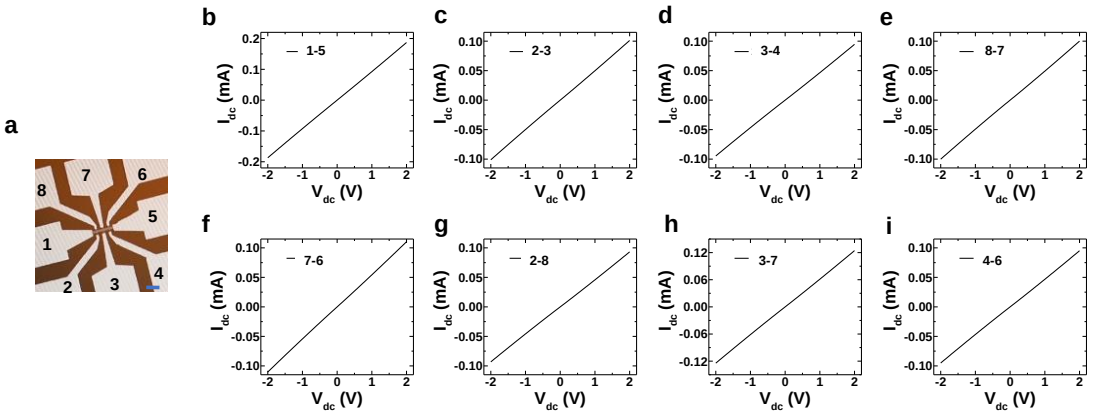

Supplementary Figure 10. Two-terminal DC measurements in 20 SL $MnBi_2Te_4$

device. (a) Optical image of the Hall-bar device. Scale bar, 50 μm. (b) Two-terminal *I*-*V* curves for different configurations.

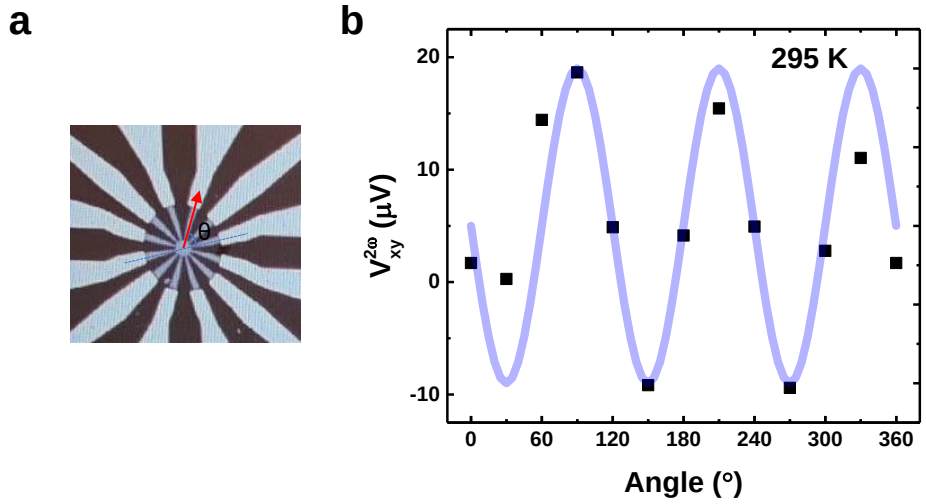

Supplementary Figure 11. Angular dependence of the nonlinear transverse signal in 20 SL $MnBi_2Te_4$ device. (a) Optical image of the device with radially distributed electrodes. (b) Second-harmonic transverse response $V_{xy}^{2\omega}$ as a function of the current injection angle.

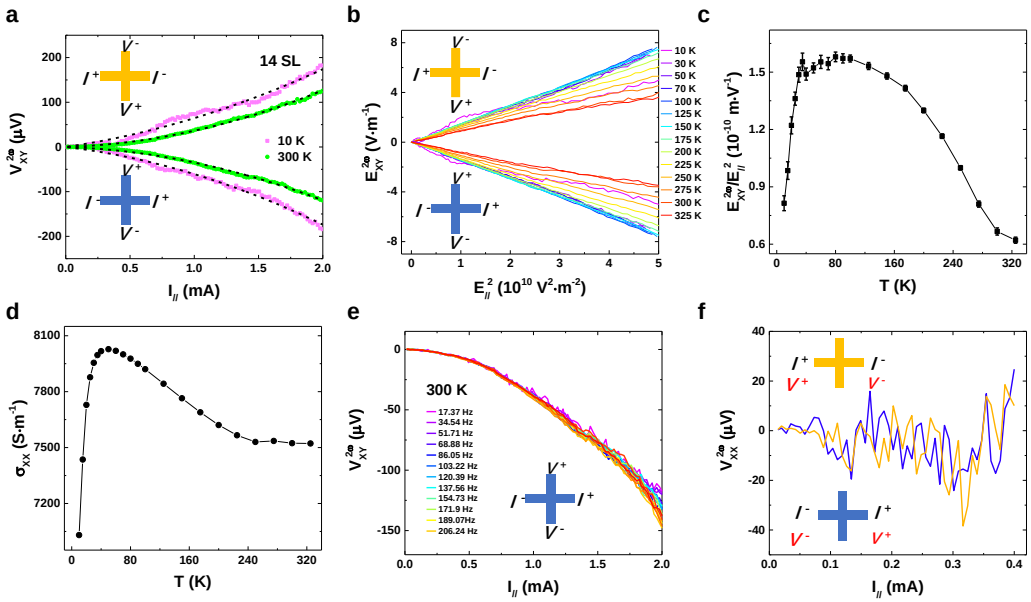

Supplementary Figure 12. Room-temperature nonlinear transverse response in 14 SL $MnBi_2Te_4$ device. (a) Nonlinear transverse response $V_{xy}^{2\omega}$ as a function of current at 10 K and 300 K for two measurement configurations with opposite current injection. Dash lines are the quadratic fittings. (b) Linear dependence of $E_{xy}^{2\omega}$ versus $E_{//}^2$ at varying temperatures. (c) Temperature-dependent nonlinear transverse magnitude $\frac{E_{xy}^{2\omega}}{E_{//}^2}$. The error bars are added based on the standard fitting error of $E_{xy}^{2\omega}$ versus $E_{//}^2$. (d)

Longitudinal conductivity σ_{xx} as a function of temperature. (e) Frequency-dependent $V_{xy}^{2\omega}$ measured at 300 K. (f) $V_{xx}^{2\omega}$ as a function of current measured at 300 K.

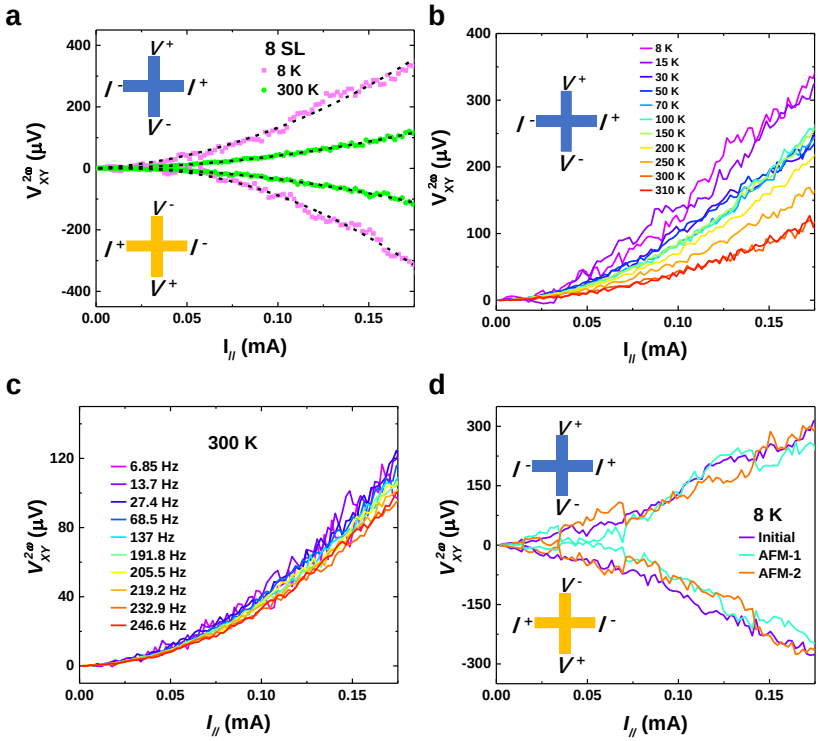

Supplementary Figure 13. Room-temperature nonlinear transverse response in 8 SL $MnBi_2Te_4$ device. (a) Typical pair of nonlinear transverse response $V_{xy}^{2\omega}$ as a function of current obtained under two measurement setups. Dash lines are the quadratic fittings. (b) Temperature-dependent nonlinear signals. (c) Frequency-dependent $V_{xy}^{2\omega}$ obtained at 300 K. (d) Comparison of nonlinear transverse response obtained at three magnetic states.

Supplementary Note 5. Additional microwave rectification data

Supplementary Figure 14a shows the 2D mapping of rectified DC voltage (V_{xy}^{dc}) as a function of RF frequency (f_{IN}) and power (P_{IN}), which demonstrates a broad response within 1-3 GHz. Supplementary Figure 14b shows some representative rectified curves, and with the RF power increasing, the V_{xy}^{dc} increases correspondingly showing a linear dependence (Supplementary Figure 14c). The highest response is at f_{IN}=1.58 GHz.

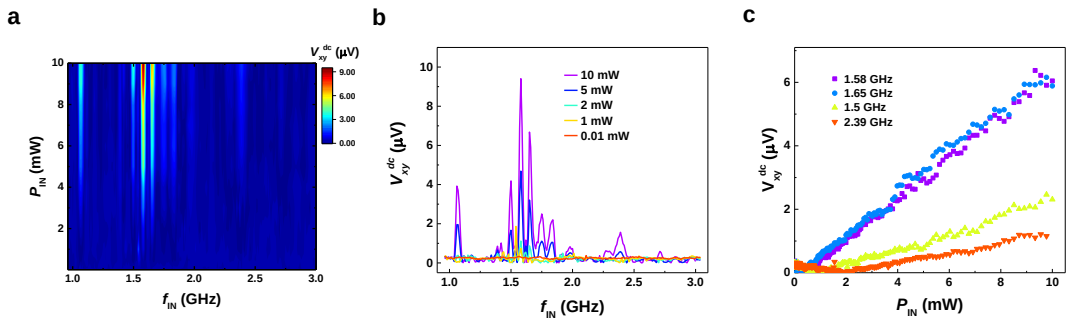

Supplementary Figure 14. Room-temperature rectification in another device along the transverse direction V_{xy}^{dc}. (a) 2D mapping plot of rectification signal as a function of radiofrequency power (P_{IN}) and frequency (f_{IN}). (b) V_{xy}^{dc} as a function of the frequency at different powers. The highest response is located at f_{IN}=1.58 GHz. (c) Linear relation between V_{xy}^{dc} and P_{IN} at different frequencies. radiofrequency power.

Supplementary References

1. Atencia, R. B., Xiao, D. & Culcer, D. Disorder in the nonlinear anomalous Hall effect of PT-symmetric Dirac fermions. *Phys. Rev. B* **108**, L201115 (2023).
2. Culcer, D., Sekine, A. & MacDonald, A. H. Interband coherence response to electric fields in crystals: Berry-phase contributions and disorder effects. *Phys. Rev. B* **96**, 035106 (2017).
3. Atencia, R. B., Niu, Q. & Culcer, D. Semiclassical response of disordered conductors: Extrinsic carrier velocity and spin and field-corrected collision integral. *Phys. Rev. Res.* **4**, 013001 (2022).
4. Wang, J. & Culcer, D. Suppression of the Kondo resistivity minimum in topological insulators. *Phys. Rev. B* **88**, 125140 (2013).
5. Parente, V., Tagliacozzo, A., von Oppen, F. & Guinea, F. Electron-phonon interaction on the surface of a three-dimensional topological insulator. *Phys. Rev. B* **88**, 075432 (2013).
6. Fonseca, J. *et al.* Anomalous Second Harmonic Generation from Atomically Thin MnBi2Te4. *Nano Lett.* **22**, 10134–10139 (2022).
7. Li, J. *et al.* Intrinsic magnetic topological insulators in van der Waals layered MnBi2Te4-family materials. *Sci. Adv.* **5**, eaaw5685 (2019).
8. Otrokov, M. M. *et al.* Prediction and observation of an antiferromagnetic topological insulator. *Nature* **576**, 416–422 (2019).
9. Chen, Y. J. *et al.* Topological Electronic Structure and Its Temperature Evolution in Antiferromagnetic Topological Insulator MnBi2Te4. *Phys. Rev. X* **9**, 041040 (2019).
10. Huang, Z., Du, M.-H., Yan, J. & Wu, W. Native defects in antiferromagnetic topological insulator MnBi2Te4. *Phys. Rev. Mater.* **4**, 121202 (2020).
11. Du, M.-H., Yan, J., Cooper, V. R. & Eisenbach, M. Tuning Fermi Levels in Intrinsic Antiferromagnetic Topological Insulators MnBi2Te4 and MnBi4Te7 by Defect Engineering and Chemical Doping. *Adv. Funct. Mater.* **31**, 2006516 (2021).
12. He, M. *et al.* Intrinsic and extrinsic dopings in epitaxial films MnBi2Te4. *J. Phys.: Condens. Matter* **35**, 295701 (2023).
13. Deng, Y. *et al.* Quantum anomalous Hall effect in intrinsic magnetic topological insulator MnBi2Te4. *Science* **367**, 895–900 (2020).
14. Li, Y., Zou, X., Li, J. & Zhou, G. Ferromagnetism and topological surface states of manganese doped Bi2Te3: Insights from density-functional calculations. *J. Chem. Phys.* **140**, 124704 (2014).
15. Hor, Y. S. *et al.* Development of ferromagnetism in the doped topological insulator Bi2−xMnxTe3. *Phys. Rev. B* **81**, 195203 (2010).

16. Lee, J. S. *et al.* Ferromagnetism and spin-dependent transport in n-type Mn-doped bismuth telluride thin films. *Phys. Rev. B* **89**, 174425 (2014).
17. Nandy, S. & Sodemann, I. Symmetry and quantum kinetics of the nonlinear Hall effect. *Phys. Rev. B* **100**, 195117 (2019).
18. Liu, H. *et al.* Intrinsic Second-Order Anomalous Hall Effect and Its Application in Compensated Antiferromagnets. *Phys. Rev. Lett.* **127**, 277202 (2021).
19. Zhang, C.-P., Gao, X.-J., Xie, Y.-M., Po, H. C. & Law, K. T. Higher-order nonlinear anomalous Hall effects induced by Berry curvature multipoles. *Phys. Rev. B* **107**, 115142 (2023).
20. Gao, A. *et al.* Quantum metric nonlinear Hall effect in a topological antiferromagnetic heterostructure. *Science* **381**, 181–186 (2023).
21. Lai, S. *et al.* Third-order nonlinear Hall effect induced by the Berry-connection polarizability tensor. *Nat. Nanotechnol.* **16**, 869–873 (2021).
22. Du, Z. Z., Lu, H.-Z. & Xie, X. C. Nonlinear Hall effects. *Nat. Rev. Phys.* **3**, 744–752 (2021).
23. Liu, H. *et al.* Berry connection polarizability tensor and third-order Hall effect. *Phys. Rev. B* **105**, 045118 (2022).
24. Ye, X.-G. *et al.* Orbital polarization and third-order anomalous Hall effect in WTe2. *Phys. Rev. B* **106**, 045414 (2022).